Ultrathin Terahertz Triple-Band Metamaterial Absorbers: Consideration of Interlayer Coupling

Chunxu Chen,[1] Sultan Can,[1,2] Jacob Schalch,[3] Xiaoguang Zhao,[1] Guangwu Duan,[1] Richard D. Averitt,[3,†] and Xin Zhang[1,*]

[1] *Department of Mechanical Engineering, Boston University, Boston, Massachusetts 02215, USA*
[2] *Department of Electrical and Electronics Engineering, Ankara University, Ankara 06830, Turkey*
[3] *Department of Physics, University of California, San Diego, La Jolla, California 92093, USA*

(Received 4 August 2020; revised 27 September 2020; accepted 5 October 2020; published 11 November 2020)

We present a polarization-insensitive air-spaced triple-band metamaterial perfect absorber (MMPA), consisting of a metamaterial layer and metallic ground plane operating at terahertz frequencies. Three near-unity absorption peaks can be individually determined by the geometry of the ring resonators within one unit cell, since the inter-unit-cell coupling is negligible. However, for sufficiently small interlayer spacing ($\lesssim 20\ \mu$m), coupling between the metamaterial layer and the ground plane is non-negligible. Therefore, near-field interactions must be taken into account for a full understanding of the electromagnetic response (EMR). Interference theory is often used to model the EMR of MMPAs analytically, in which interlayer coupling between the metamaterial and ground plane is usually neglected, resulting in a predicted blueshift of the absorption peaks in comparison to experiment. To account for near-field coupling, we incorporate correction terms into the analytical interference model by taking into account the effective interlayer capacitance and inductance. This results in good agreement between interference theory and experiment (and full-wave numerical simulations). Our findings demonstrate that interlayer coupling is an important design parameter for ultrathin MMPAs.

DOI: 10.1103/PhysRevApplied.14.054021

I. INTRODUCTION

In recent years, metamaterial absorbers have attracted considerable attention, with a rapid increase in research owing to numerous potential applications. Conventional electromagnetic absorbers, such as Salisbury screens and Jaumann absorbers, operating at microwave frequencies consist of a high-impedance surface, a lossless quarter-wavelength spacer layer, and metallic ground plane [1,2]. In contrast, metamaterial absorbers can operate at any desired frequency and are often dramatically subwavelength in thickness ($\sim\lambda/100$) [3–5]. Thus, metamaterial perfect absorbers (MMPAs) offer considerable advantages for various applications, such as energy harvesting [6], refractive-index sensing [7], solar cells [8], thermal emitters [9], chemical sensing [10,11], and imaging devices [12,13]. MMPAs usually have a three-layer configuration: a metamaterial and a ground plane layer separated by a very thin dielectric spacer [14,15]. With judicious design, MMPAs can be designed to exhibit polarization-insensitive absorption [16], wide-angle absorption [17,18], dual-band or multiband absorption [19,20], and broadband absorption [21]. However, many designs require multiple unit-cell designs or multilayer structures and different unit-cell orientations to satisfy multifrequency, broadband, and polarization-independent operation.

Here, a simple three-layer MMPA polarization-insensitive air-spaced triple-band absorber with a single unit-cell design is demonstrated at terahertz frequencies. To obtain a triple-band MMPA with polarization insensitivity, a symmetric unit-cell design with three ring resonators of different geometries is utilized. Furthermore, the dielectric spacer layer is replaced by air in our MMPA, resulting in relatively high Q factors for the three absorption peaks. The spacer materials are usually considered as an important component for power absorption, where most of the power dissipation occurs. By replacing the traditional dielectric spacer material with air, due to the absence of dielectric loss, a quality factor can increase more than 3 times compared with the traditional metamaterial absorber with dielectric spacer [22,23].

We utilize terahertz time-domain spectroscopy (THz TDS) to measure the reflection coefficient of the fabricated MMPAs [24] for various geometries. In particular, we investigate MMPAs in the ultrathin limit, where interlayer spacing between the metamaterial layer and ground plane in our experiments is 5 μm. As we demonstrate,

*xinz@bu.edu
†raveritt@ucsd.edu

this results in interlayer capacitive and inductive coupling, which must be considered for a full understanding of the electromagnetic response (EMR). For example, neglecting the interlayer coupling in interference theory predicts (in the ultrathin limit) a blueshift of the absorption peaks, in comparison to experiments and full-wave electromagnetic simulations. In our corrected interference theory, we include the near-field interaction between the metamaterial layer and the ground plane, which is omitted in conventional interference theory [25]. Although there are studies [26] that have already reported the difference between interference theory and experimental results in MMPAs, a detailed analysis has yet to be presented. In our approach, the effective interlayer capacitance and inductance are calculated using transmission-line modeling. Augmenting interference theory by incorporating interlayer coupling yields excellent agreement with experiments (and full-wave simulations), highlighting the need to consider such effects in MMPAs and other ultrathin metamaterial devices and structures.

II. TRIPLE-BAND METAMATERIAL ABSORBER

A. Absorber design and fabrication process

The schematic of the air-spaced triple-band MMPA is shown in Fig. 1(a). The unit cell has three independent ring resonators, which are referred to as the inner ring, middle ring, and outer ring. Finite-difference time-domain simulation (CST Microwave Studio 2017) is used to design the MMPA. A periodic boundary condition and normal incidence are used to simulate the metamaterial response. Gold is taken as a lossy metal with a conductivity of 4.56×10^7 S/m, and the silicon nitride is treated as a dielectric material from 0.4 to 2 THz with a relative permittivity of $\varepsilon = 7$. Based on simulation results, as shown in Figs. 1(e)–1(g), each ring corresponds to a unique resonance mode, corresponding to a specific peak in the absorption spectrum, as indicated by red, green, and blue lines. [Fig. 1(d)]. Since each ring only corresponds to a single absorption peak, the in-plane coupling among the rings is negligible. This is evident by the near-perfect overlap between the simulations of the individual resonators (colored lines) and the simulations of all three resonators at once (black dashed line). As can be clearly observed in Fig. 1(d), the three distinct absorption peaks are at 0.86, 1.23, and 1.77 THz, with the structural parameters in design (a), as listed in Table I. Detailed structural parameters for the four different designs we test are shown in Table. I.

The MMPA structures are fabricated with two wafer processes and flip-chip bonding. The first wafer is silicon coated through low-pressure chemical vapor deposition with silicon nitride films on both sides. The metamaterial unit cells are defined on the front side of the first wafer using photolithography and lift-off processes.

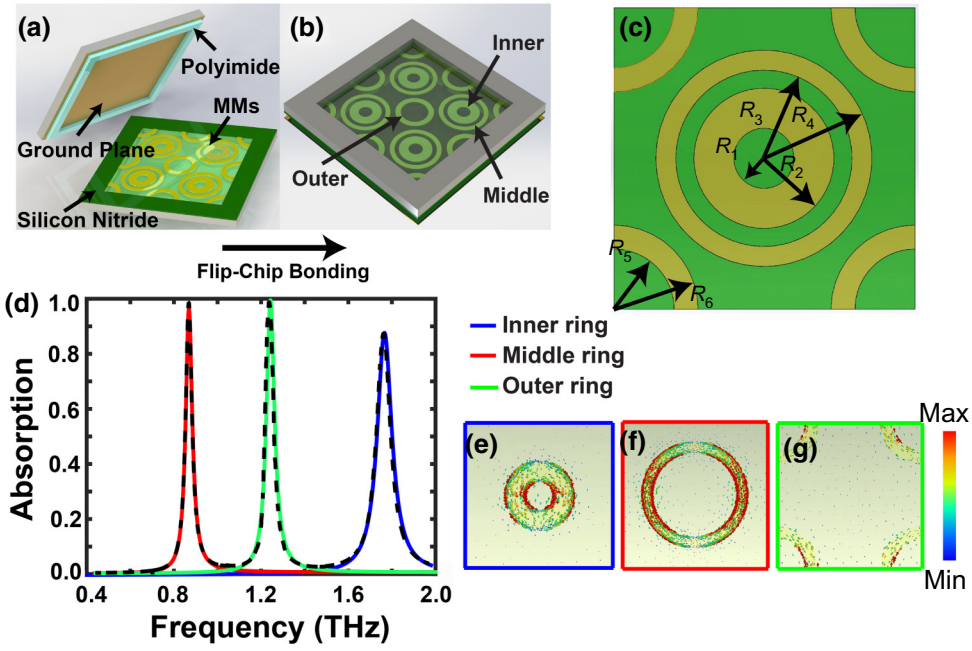

FIG. 1. (a),(b) Metamaterial structure of the air-spaced triple-band metamaterial absorber. (c) Unit-cell structure of the triple-band air-spaced metamaterial absorber. (d) Simulations of the air-spaced triple-band metamaterial absorber. Simulation results of the EMR for the air-spaced triple-band metamaterial absorber (dashed black line), with each ring corresponding to a distinct absorption peak. Separate simulations of each individual ring are shown for the inner ring (blue line), the middle ring (red line), and the outer ring (green line), showing excellent correspondence with the full triple-band simulation. On-resonance surface current for three different modes: (e) inner ring (1.77 THz), (f) middle ring (0.86 THz), and (g) outer ring (1.23 THz).

TABLE I. Structural parameters for four different designs of air-spaced triple-band metamaterial absorber. R_1 and R_2, R_3 and R_4, and R_5 and R_6 are the inner and outer radii parameters for inner circles, middle circles, and outer circles, respectively. By changing the radius of each circle, the absorption peaks will change accordingly. The air-spacer thickness is 5 μm and the SiN_x thickness is 400 nm in all designs.

Metamaterial structural parameters						
Design	R_1 (μm)	R_2 (μm)	R_3 (μm)	R_4 (μm)	R_5 (μm)	R_6 (μm)
a	15	35	44	54	30	42
b	15	35	44	54	25	42
c	15	35	44	58	30	42
d	18	35	44	54	30	42

Subsequently, the wafer is etched thoroughly under the metamaterial area using potassium hydroxide wet etching. For the second wafer, gold is deposited on the silicon substrate to serve as a ground plane. Then, the polyimide bonding pads are patterned on the second wafer. Finally, the two wafers are subsequently integrated using a flip-chip bonder (FC-150). The final sample images and detailed fabrication process flow are presented in Appendix A.

B. Experimental results

The fabricated samples are characterized using THz TDS in reflection at normal incidence. The reference signal is measured from a gold-coated silicon substrate. The experimental results are shown in Fig. 2(a). Crucially, with changes in one ring radius, the relevant absorption peak will shift, while the others will not. As shown in Fig. 2(b), when the inner radius (R_1) is increased from 15 to 18 μm, the high-frequency absorption peak shifts from 1.77 to 1.66 THz, while the other peaks remain the same. In a similar way, as shown in Fig. 2(c), when the middle radius (R_4) is increased from 54 to 58 μm, the low-frequency absorption peak shifts from 0.86 to 0.81 THz. Likewise, as seen in Fig. 2(d), when the outer radius (R_5) is decreased from 30 to 25 μm, the middle absorption peak shifts from 1.23 to 1.37 THz, while the other peaks remain unchanged. The experimental results for different geometries demonstrate that the resonant frequency of each mode can be controlled by the radius of the corresponding ring without altering the other resonances, indicating weak in-plane coupling between the rings in each unit cell. As a result, the absorption peak frequencies can be independently changed. The simulation (and experimental) quality factors (Q) for each absorption peak are 26 (14) at 0.86 THz, 32 (19) at 1.23 THz, and 25 (12) at 1.77 THz. The major difference between simulation (red) and experimental (green) results is likely to arise from

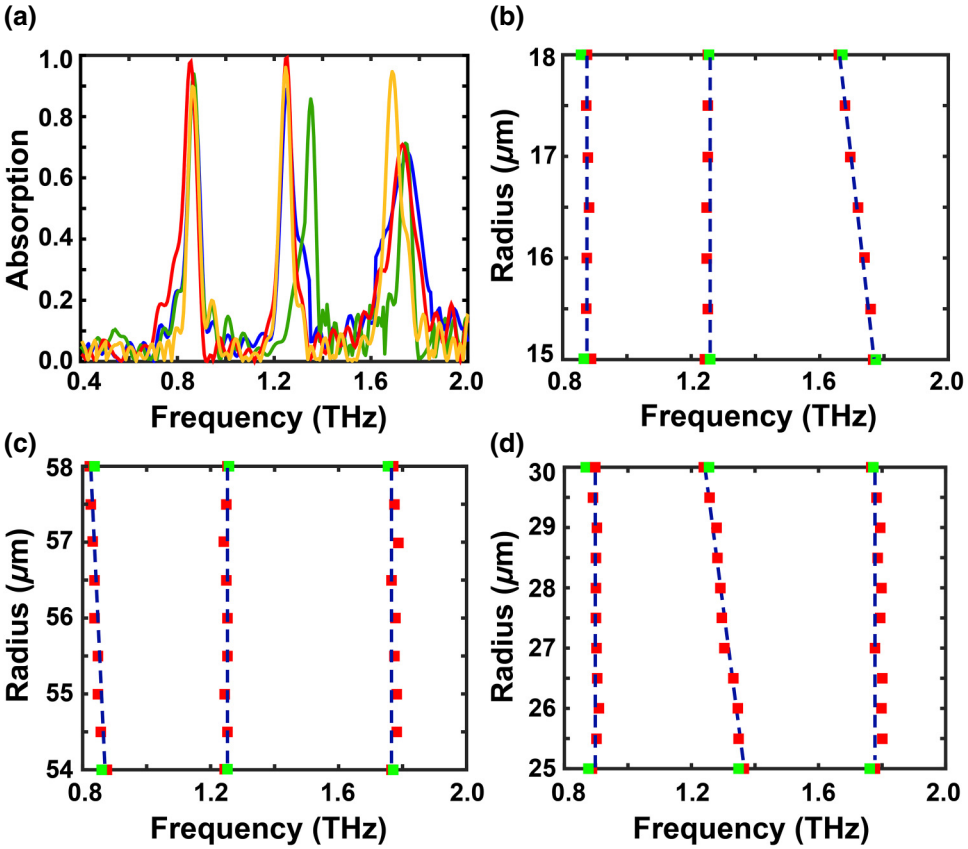

FIG. 2. Experimental results and simulations of fabricated MMPAs. (a) Experimental results for four different designs listed in Table I. Blue, design a; green, design b; red, design c; and orange, design d. (b)–(d) Simulations of shifting of the absorption peaks as the radius is changed in the metamaterial structure. Red squares show simulation results of absorption peaks for different radii, while green squares show experimental results. Blue dashed lines are a guide to the eye.

slight errors in the reflection measurement and fabrication defects in photolithography and lift-off processes. Compared with conventional absorbers with dielectric spacers, the air-spacer triple-band absorber exhibits higher Q values for all three peaks, which could be useful in THz sensing applications [27].

III. INTERFERNECE THEORY AND INTERLAYER COUPLING

A. Interference theory

With the basic description of the EMR of the absorbers presented above, we now proceed to our main results related to interlayer coupling. We start with a detailed analysis of the results using interference modeling. The interference model is a well-developed theory to analytically calculate the reflection of the metamaterial absorbers [21,28]. For example, interference theory can accurately predict the response of MMPAs consisting of split-ring resonators over a ground plane [27,29,30]. Initially, we use conventional interference theory to calculate the EMR of our MMPAs. By calculating the superposition of multiple reflections from the ground plane and metamaterial layer, the overall reflection can be easily calculated with the following equation [25],

$$r = r_{\mathrm{MM}} - t_{\mathrm{MM}}^2 e^{i2\beta}/(1 + r_{\mathrm{MM}} e^{i2\beta}), \tag{1}$$

where r is the overall reflection and $\beta = nkd$ is the one-way phase delay arising from the spacer layer. In our absorber design, the refractive index of the spacer, i.e., air, is $n = 1$; k is the wave number in vacuum; and d is the air-spacer thickness (i.e., the interlayer distance between the metamaterial layer and ground plane). In Eq. (1), r_{MM} (t_{MM}) denotes the complex reflection (transmission) coefficient of the metamaterial layer without a ground plane, which may be directly obtained from simulations.

With the simulated r_{MM}, t_{MM}, and other known parameters from the air-spaced triple-band absorber designs, the absorption response is calculated using Eq. (1), and the results are shown in Fig. 3 [orange dashed line, design (a) in Table I]. When compared with full-wave electromagnetic simulations (blue solid line in Fig. 3) and experimental results (green dashed line), the prediction using interference modeling exhibits higher resonance frequencies for all of the modes. Clearly, in the air-spaced triple-band absorber design, the direct adoption of interference theory does not agree (in the ultrathin limit) with either simulation or experiments. Therefore, an improved model is needed to describe the MMPA analytically. In the interference model [Eq. (1)], near-field coupling between the metamaterial layer and the ground plane is not considered, yet may be critical in determining the absorption response when the spacer thickness is thin [28]. Indeed, the stark difference between the interference model with the simulation and experimental results suggests that near-field interactions between the ground plane and the metamaterial layer are significant in our MMPAs.

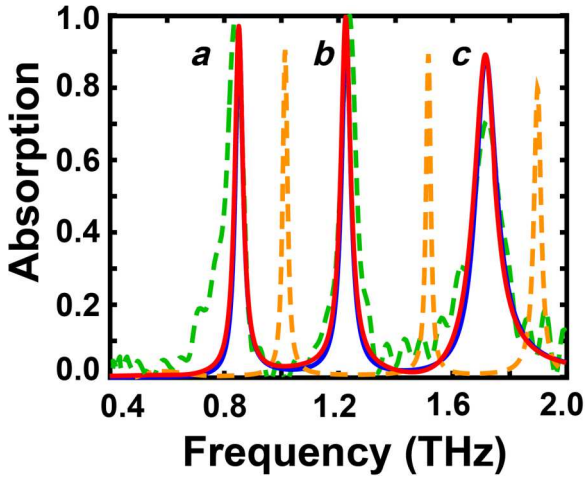

FIG. 3. Comparison between experiment, full-wave electromagnetic simulation, and interference theory; *a*, *b*, and *c* refer to different resonance peaks. Experimental results (green dashed line) of the air-spacer triple-band absorber with structural parameters of design a in Table I. Full-wave electromagnetic simulations (blue line) exhibit good agreement with theory. Uncorrected interference modeling (orange dashed line) predicts resonances that are blueshifted. Upon taking into account coupling, as manifested in interlayer capacitance and inductance, the calculated absorption using augmented interference theory (red line) agrees with experiments and simulation.

B. Interlayer capacitance and inductance

In the following, we quantitatively investigate the interlayer capacitance and inductance. This is accomplished using an analytical transmission-line model [31,32] of the air-spaced triple-band metamaterial structures to calculate the complex reflection and transmission coefficients. The three absorption peaks can be modeled as distinct *RLC* circuits with

$$Z_i = R_i + i\omega L_i + 1/i\omega C_i, \tag{2}$$

where Z_i, R_i, L_i, and C_i are the impedance, resistance, inductance, and capacitance, respectively, for each ring, where the subscript $i = a$, b, and c represents each peak (see labels in Fig. 3). The first term on the right-hand side of Eq. (2), R_i, is the equivalent resistance of the metamaterial gold rings, representing the ohmic loss in the metallic unit cells. The equivalent inductance, L_i, and capacitance, C_i, are the effective reactance of each ring. The values of the resistance, R_i; inductance, L_i; and capacitance, C_i, can be analytically fitted with Eq. (3), in which the S parameters (S_{11}, S_{12}, S_{21}, and S_{22}) are all obtained from the numerical simulation. Consequently, by using the

transmission-line model, the complex coefficients r_{MM} and t_{MM} can be derived from the impedance model for each ring

$$\begin{bmatrix} r_{MM} & t_{MM} \\ t_{MM} & r_{MM} \end{bmatrix} = \begin{bmatrix} S_{11} & S_{12} \\ S_{21} & S_{22} \end{bmatrix} = 1/(2Z_i + Z_0) \begin{bmatrix} -Z_0 & 2Z_i \\ 2Z_i & -Z_0 \end{bmatrix}, \quad (3)$$

where Z_0 is the free-space impedance. Since the in-plane coupling is negligible in our design, Z_i can be replaced in a similar way for different rings. After r_{MM} and t_{MM} are obtained from Eq. (3), the reflection and transmission coefficients can be inserted into the interference model, Eq. (1), to calculate the overall reflection of the MMPA. In this way, the impedance within the system can be retrieved for each ring, with the help of the MATLAB curve-fitting functions. More importantly, the capacitance and inductance of the MMPA without and with the ground plane can be calculated independently by substituting the results from Eq. (3), i.e., r_{MM} and t_{MM}, into that for interference theory, Eq. (1). No near-field interaction needs to be considered when there is only one layer of rings (MMs) and the air spacer. Under these circumstances, the total capacitance (inductance) is just the intrinsic resonator capacitance (inductance) from the metamaterial rings, which is defined as C_{MM} (L_{MM}). However, when there is a gold ground plane to create the absorber structure, the near-field interaction between the metamaterial layer and the ground plane will result in an interlayer capacitance (inductance) in parallel with the intrinsic ring capacitance (inductance). Under such conditions, the overall capacitance (inductance) is defined as C_{MMPA} (L_{MMPA}).

The absorption spectra of the air-spaced triple-band absorbers calculated from corrected interference theory is shown in Fig. 3 (red curve). When the near-field interactions are incorporated into the interference model, the capacitance increases from 4.01×10^{-16} to 7.95×10^{-16} F for the lower absorption peaks at 0.87 THz. As expected, the inductance decreases from 5.37×10^{-11} to 3.51×10^{-11} H, because the surface current is in the opposite direction on the ground plane and metamaterial layer. The resistance (R), inductance (L), and capacitance (C) parameters for each peak with and without a ground plane are shown in Table II for an air-spacer thickness of 5 μm. The capacitance increases and the inductance decreases when taking into account interlayer coupling. More importantly, with the transmission-line model and interference theory, the interlayer capacitance originating from the near-field interactions between the ground plane and the metamaterial layer can be numerically calculated. The interlayer capacitances and inductances for each rings are shown in Table II for peaks a, b, and c.

Qualitatively, coupling between the metamaterial layer and the gold ground plane yields an interlayer capacitance parallel to the resonator capacitance and interlayer inductance in series of the resonator inductance for different rings (see Appendix B for the equivalent circuit). Therefore, the total capacitance of the MMPA will increase, decreasing the absorption frequency in comparison to when this is not taken into account (i.e., in interference modeling). It is also expected that the coupling of this frequency shift will become smaller with increasing air-spacer thickness. Furthermore, interlayer coupling-induced frequency shifts will not be as dramatic in some types of metamaterials, such as split-ring resonator (SRR) based MMPAs. This is because the capacitance of SRRs is much larger than that of the interlayer capacitance. As a result, the calculated interference peak absorption frequency agrees well with the experimental and simulation results in previous studies, even though coupling between the MMs and the ground plane is not considered [33–35].

C. Spacer-thickness dependence

For our MMPA, the near-field interlayer coupling is highly dependent on the spacer thickness [20]. Figure 4 presents a color map, showing the evolution of the absorption spectra resonance frequency for different air-spacer thicknesses obtained using full-wave simulations. The green solid lines show conventional interference theory from Eq. (1), without taking into account the interlayer coupling, and the white dashed line shows the peak

TABLE II. Values of resistance (R), inductance (L), capacitance (C) with and without the ground plane, and interlayer capacitance (C_{IL}) and inductance (L_{IL}) for each peak for an air-spacer thickness of 5 μm.

RLC for each peak with and w/o ground plane								
	W/o ground plane			With ground plane			Interlayer C and L	
Peak	R_{MM} (Ω)	L_{MM} (H) $\times 10^{-11}$	C_{MM} (F) $\times 10^{-16}$	R_{MMPA} (Ω)	L_{MMPA} (H) $\times 10^{-11}$	C_{MMPA} (F) $\times 10^{-16}$	L_{IL} (H) $\times 10^{-11}$	C_{IL} (F) $\times 10^{-16}$
a	2.70	5.37	4.01	3.50	3.51	7.95	−1.86	3.94
b	3.00	5.38	1.84	5.30	2.78	5.08	−2.60	3.24
c	9.00	8.08	0.82	7.20	1.54	4.44	−6.54	3.62

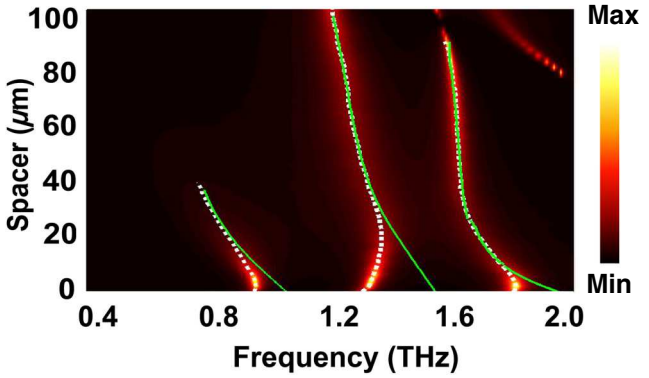

FIG. 4. Absorption diagram as a function of air-spacer layer thickness from 2 to 100 μm. Absorption peaks of interference theory without correction (green solid line) and simulation results (white dashed line).

frequency for each resonance from the simulations. Differences between full-wave simulations in conventional interference theory are especially clear when the air-spacer thickness is less than 20 μm. In this regime, the calculated absorption peak frequencies using interference modeling are much higher than the simulation peaks. However, when the air-spacer thickness is larger than 40 μm, the calculated results match the peak absorption frequency obtained from simulation, suggesting that near-field interactions are very weak in this range. In short, beyond a critical spacer thickness, the interlayer capacitance from the ground plane and the metamaterial layer is negligible compared with the capacitance within the metamaterial layer (see Appendix C for the cross-section electric field plot).

IV. CONCLUSION

We present an air-spacer triple-band absorber with a high Q factor and independent tuning for each peak. Since the near-field interaction is omitted in conventional interference theory, it cannot accurately predict the electromagnetic response of our multiband absorber, which is in the ultrathin limit and, therefore, exhibits significant interlayer capacitive and inductive coupling between the metamaterial layer and the ground plane. Indeed, we demonstrate that the effective increase in the capacitance and decrease in the inductance are the primary sources of the difference between conventional interference theory and simulation and experimental results. We also illustrate that the spacer thickness is a crucial factor to consider, especially in the ultrathin limit (defined as when significant interlayer coupling occurs). Using transmission-line modeling in conjunction with interference theory, interference modeling can be used to obtain good agreement with full-wave simulations. Furthermore, the interlayer capacitance and inductance can be accurately calculated in our approach and reveal that coupling between the metamaterial layer and the ground plane is very strong in our absorber design. The corrected interference theory derived above can be directly used in many absorber designs and applications to predict the absorption spectra, especially for those without traditional SRR structures and with thin spacer layers.

ACKNOWLEDGMENTS

We acknowledge support from the National Science Foundation (NSF) (Grant No. ECCS-1810252). Work at UCSD is supported by the Army Research Office under Grant No. MURI W911NF-16-1-0361. We thank the Boston University Photonic Center for technical support. S.C. also acknowledges TUBITAK for supporting her stay at Boston University during her Ph.D. studies through Program 2214A.

APPENDIX A: PROCESS FLOW AND SAMPLE PICTURES

Ultrathin terahertz triple-band metamaterial absorbers are fabricated through two-wafer processes. The detailed process flow is shown in Fig. 5. The optical microscopy

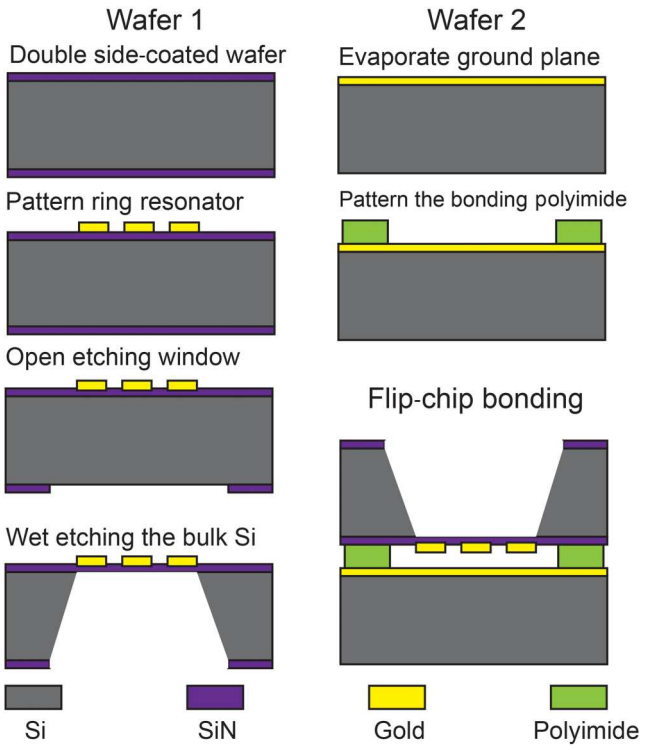

FIG. 5. Fabrication process of triple-band MMPA. Two wafers are employed for fabrication. Triple-ring structures (MMs) are patterned through photolithography and lift-off processing on the first wafer, while the second wafer acts as the gold ground plane. Two wafers are bonded with a flip-chip bonder (FC-150).

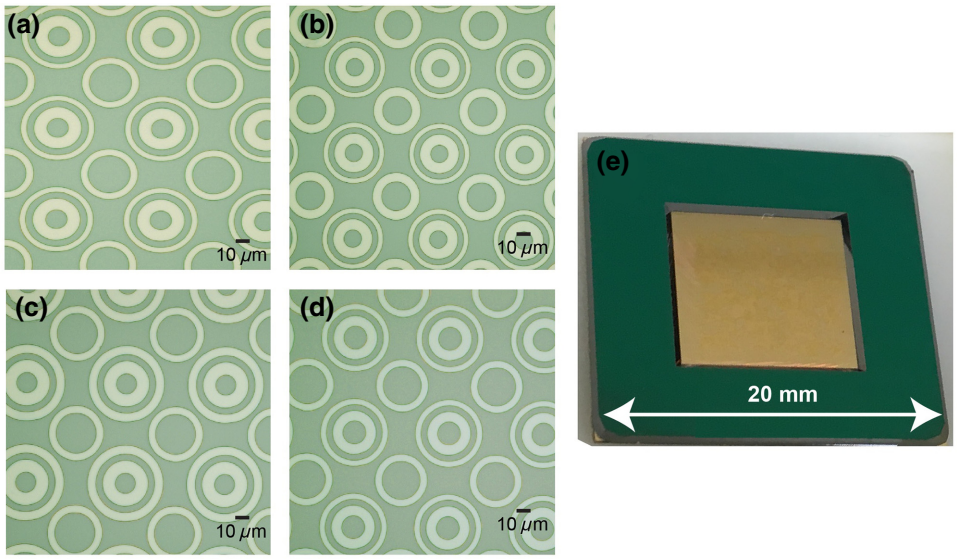

FIG. 6. (a)–(d) Optical microscopy images for four different designs (detailed structural parameters are shown in Table I). (e) Image of the final fabricated ultrathin metamaterial absorber.

images of the MMPA for four different designs are shown in Figs. 6(a)–6(d), while the final sample image is shown in Fig. 6(e). The final sample is 20×20 mm^2.

APPENDIX B: EQUIVALENT CIRCUIT FOR METAMATERIAL ABSORBER

Based on the transmission-line model and interference theory, the interlayer capacitance (C_p) and inductance (L_p) can be derived for each ring. The impedance for each ring can be divided into three parts: resistance (R), inductance (L), and capacitance (C). As shown in Fig. 7, when the interlayer coupling is considered, the interlayer capacitance (C_{IL}) is parallel to the resonator capacitance (C_{MM}),

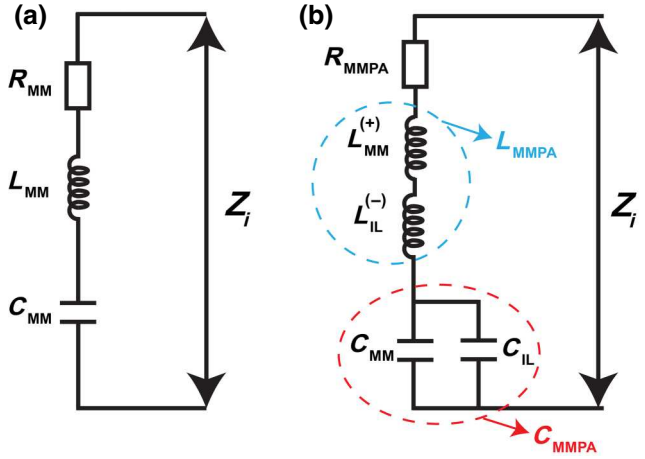

FIG. 7. Simplified circuit model of ultrathin MMPA. (a) Without consideration of interlayer coupling, impedance for each ring (Z_i) can be modeled as intrinsic resistance (R_{MM}), inductance (L_{MM}), and capacitance (C_{MM}). (b) Near-field coupling is incorporated in transmission-line model; impedance for each ring can be modeled with the overall resistance (R_{MMPA}), inductance (L_{MMPA}), and capacitance (C_{MMPA}).

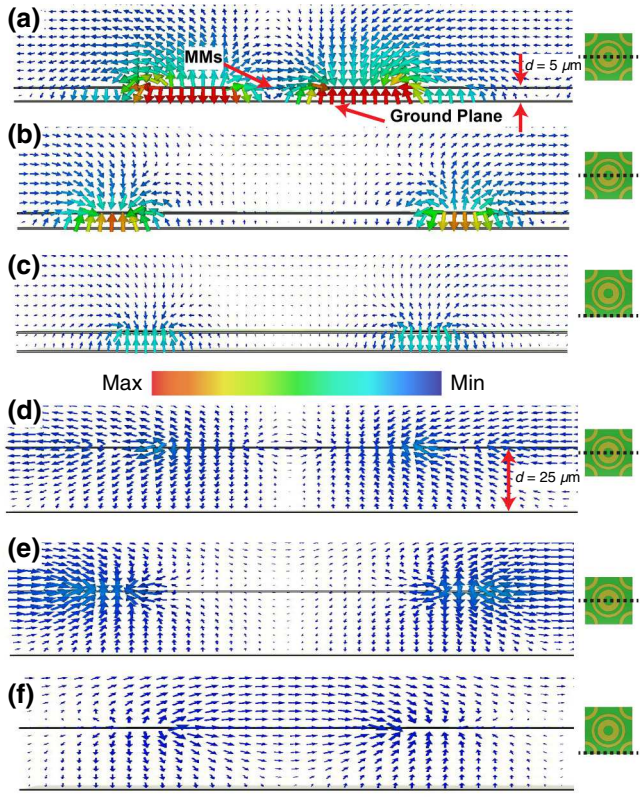

FIG. 8. Cross-section view of electric field distribution for three resonance peaks with different spacer thicknesses. Selected cross sections are depicted by dashed lines on the right, for each of the different rings. Air-spacer thickness of 5 μm: (a) inner ring at 1.77 THz, (b) middle ring at 1.23 THz, and (c) outer ring at 0.86 THz. Air-spacer thickness of 25 μm: (d) inner ring at 1.63 THz, (e) middle ring at 1.31 THz, and (f) outer ring at 0.77 THz.

while the interlayer inductance (L_{IL}) is connected in series to the resonator inductance (L_{MM}), but with the opposite current direction.

APPENDIX C: CROSS-SECTION ELECTRIC FIELD PLOT

The electric field distribution of the MMPA with different air-spacer thicknesses are shown in Fig. 8. For the thin spacer thickness (e.g., 5 μm), as depicted in Figs. 8(a)–(c), the electric field intensity is clearly much stronger than that with a thick spacer thickness (e.g., 25 μm), as depicted in Figs. 8(d)–(f) for all three resonance modes. It clearly shows that the interlayer coupling between the metamaterial layer and the ground plane is more significant in the thin spacer absorber compared with the one with a thick spacer layer. It is also expected that the frequency shifts from interference theory will become smaller with increasing air-spacer thickness, due to a decrease in interlayer coupling.

[1] F. Costa, A. Monorchio, and G. Manara, Analysis and design of ultra thin electromagnetic absorbers comprising resistively loaded high impedance surfaces, IEEE Trans. Antennas Propag. **58**, 1551 (2010).

[2] B. Munk, P. Munk, and K. Pryor, On designing jaumann and circuit analog absorbers (CA absorbers) for oblique angle of incidence, IEEE Trans. Antennas Propag. **55**, 186 (2007).

[3] H. Tao, N. I. Landy, C. M. Bingham, X. Zhang, R. D. Averitt, and W. J. Padilla, A metamaterial absorber for the terahertz regime: Design, fabrication and characterization, Opt. Express **16**, 7181 (2008).

[4] F. Ding, Y. Cui, X. Ge, Y. Jin, and S. He, Ultra-broadband microwave metamaterial absorber, Appl. Phys. Lett. **100**, 103506 (2012).

[5] X. Zhao, C. Chen, A. Li, G. Duan, and X. Zhang, Implementing infrared metamaterial perfect absorbers using dispersive dielectric spacers, Opt. Express **27**, 1727 (2019).

[6] M. Carrara, M. R. Cacan, J. Toussaint, M. J. Leamy, M. Ruzzene, and A. Erturk, Metamaterial-inspired structures and concepts for elastoacoustic wave energy harvesting, Smart Mater. Struct. **22**, 065004 (2013).

[7] N. Vasilantonakis, G. A. Wurtz, V. A. Podolskiy, and A. V. Zayats, Refractive index sensing with hyperbolic metamaterials: Strategies for biosensing and nonlinearity enhancement, Opt. Express **23**, 14329 (2015).

[8] Y. Wang, T. Sun, T. Paudel, Y. Zhang, Z. Ren, and K. Kempa, Metamaterial-plasmonic absorber structure for high efficiency amorphous silicon solar cells, Nano Lett. **12**, 440 (2012).

[9] X. Liu, T. Tyler, T. Starr, A. F. Starr, N. M. Jokerst, and W. J. Padilla, Taming the Blackbody with Infrared Metamaterials as Selective Thermal Emitters, Phys. Rev. Lett. **107**, 045901 (2011).

[10] A. V. Kabashin, P. Evans, S. Pastkovsky, W. Hendren, G. A. Wurtz, R. Atkinson, R. Pollard, V. A. Podolskiy, and A. V. Zayats, Plasmonic nanorod metamaterials for biosensing, Nat. Mater. **8**, 867 (2009).

[11] X. Hu, G. Xu, L. Wen, H. Wang, Y. Zhao, Y. Zhang, D. R. S. Cumming, and Q. Chen, Metamaterial absorber integrated microfluidic terahertz sensors, Laser Photon. Rev. **10**, 962 (2016).

[12] X. Liu, T. Starr, A. F. Starr, and W. J. Padilla, Infrared Spatial and Frequency Selective Metamaterial with Near-Unity Absorbance, Phys. Rev. Lett. **104**, 207403 (2010).

[13] C. M. Watts, D. Shrekenhamer, J. Montoya, G. Lipworth, J. Hunt, T. Sleasman, S. Krishna, D. R. Smith, and W. J. Padilla, Terahertz compressive imaging with metamaterial spatial light modulators, Nat. Photonics **8**, 605 (2014).

[14] N. I. Landy, S. Sajuyigbe, J. J. Mocj, D. R. Smith, and W. J. Padilla, Perfect Metamaterial Absorber, Phys. Rev. Lett. **100**, 207402 (2008).

[15] X. Zhao, K. Fan, J. Zhang, H. R. Seren, G. D. Metcalfe, M. Wraback, R. D. Averitt, and X. Zhang, Optically tunable metamaterial perfect absorber on highly flexible substrate, Sens. Actuator A-Phys. **231**, 74 (2015).

[16] Y. Ma, Q. Chen, J. Grant, S. C. Saha, A. Khalid, and D. R. S. Cumming, A terahertz polarization insensitive dual band metamaterial absorber, Opt. Lett. **36**, 945 (2011).

[17] X. Zhang, H. Liu, and L. Li, Tri-band miniaturized wide-angle and polarization-insensitive metasurface for ambient energy harvesting, Appl. Phys. Lett. **111**, 071902 (2017).

[18] M. Wu, X. Zhao, J. Zhang, J. Schalch, G. Duan, K. Cremin, R. D. Averitt, and X. Zhang, A three-dimensional all-metal terahertz metamaterial perfect absorber, Appl. Phys. Lett. **111**, 051101 (2017).

[19] H. Tao, C. M. Bingham, D. Pilon, K. Fan, A. C. Strikwerda, D. Shrekenhamer, W. J. Padilla, X. Zhang, and R. D. Averitt, A dual band terahertz metamaterial absorber, J. Phys. D: Appl. Phys. **43**, 225102 (2010).

[20] B. Wang, X. Zhai, G. Wang, W. Huang, and L. Wang, A novel dual-band terahertz metamaterial absorber for a sensor application, J. Appl. Phys. **117**, 014504 (2015).

[21] S. Liu, H. Chen, and T. J. Cui, A broadband terahertz absorber using multi-layer stacked bars, Appl. Phys. Lett. **106**, 151601 (2015).

[22] C. Cen, Z. Chen, D. Xu, L. Jiang, X. Chen, Z. Yi, P. Wu, G. Li, and Y. Yi, High quality factor, high sensitivity metamaterial graphene-perfect absorber based on critical coupling theory and impedance matching, Nanomaterials **10**, 95 (2020).

[23] G. Duan, J. Schalch, X. Zhao, A. Li, R. D. Averitt, and X. Zhang, in *proceedings of the 20th International Conference on Solid-State Sensors, Actuators and Microsystems & Eurosensors XXXIII*, Berlin, Germany, (2019), pp. 2294–2297.

[24] J. Schalch, G. Duan, X. Zhao, X. Zhang, and R. D. Averitt, Terahertz metamaterial perfect absorber with continuously tunable air spacer layer, Appl. Phys. Lett. **113**, 061113 (2018).

[25] Hou-Tong Chen, Interference theory of metamaterial perfect absorbers, Opt. Express **20**, 7165 (2012).

[26] L. Huang, D. R. Chowdhury, S. Ramani, M. T. Reiten, S. N. Luo, A. K. Azad, A. J. Taylor, and H. T. Chen, Impact of resonator geometry and its coupling with ground plane on ultrathin metamaterial perfect absorbers, Appl. Phys. Lett. **101**, 101102 (2012).

[27] G. Duan, J. Schalch, X. Zhao, J. Zhang, R. D. Averitt, and X. Zhang, An air-spaced terahertz metamaterial perfect absorber, Sens. Actuator A-Phys. **280**, 303 (2018).

[28] G. Duan, J. Schalch, X. Zhao, A. Li, C. Chen, R. D. Averitt, and X. Zhang, A survey of theoretical models for terahertz electromagnetic metamaterial absorbers, Sens. Actuator A-Phys. **287**, 21 (2019).

[29] G. Duan, J. Schalch, X. Zhao, J. Zhang, R. D. Averitt, and X. Zhang, Identifying the perfect absorption of metamaterial absorbers, Phys. Rev. B **97**, 035128 (2018).

[30] G. Duan, J. Schalch, X. Zhao, J. Zhang, R. D. Averitt, and X. Zhang, Analysis of the thickness dependence of metamaterial absorbers at terahertz frequencies, Opt. Express **26**, 2242 (2018).

[31] M. P. Hokmabadi, D. S. Wilbert, P. Kung, and S. M. Kim, Design and analysis of perfect terahertz metamaterial absorber by a novel dynamic circuit model, Opt. Express **21**, 16455 (2013).

[32] M. P. Hokmabadi, M. Zhu, P. Kung, and S. M. Kim, Comprehensive study of terahertz metamaterial absorber by applying a hybrid approach on its circuit analogue, Opt. Mater. Express **5**, 1772 (2015).

[33] J. Sun, L. Liu, G. Dong, and J. Zhou, An extremely broad band metamaterial absorber based on destructive interference, Opt. Express **19**, 21155 (2011).

[34] X. Zeng, M. Gao, L. Zhang, G. Wan, and B. Hu, Design of a triple-band metamaterial absorber using equivalent circuit model and interference theory, Microw. Opt. Technol. Lett. **60**, 1676 (2018).

[35] X. Shen, Y. Yang, Y. Zang, J. Gu, J. Han, W. Zhang, and T. J. Cui, Triple-band terahertz metamaterial absorber design, experiment, and physical interpretation, Appl. Phys. Lett. **101**, 154102 (2012).